arXiv:1001.4744v1 [astro-ph.CO] 26 Jan 2010

Seven-Year Wilkinson Microwave Anisotropy Probe (WMAP[1]) Observations: Sky Maps, Systematic Errors, and Basic Results

N. Jarosik[2], C. L. Bennett[3], J. Dunkley[4], B. Gold[3], M. R. Greason[5], M. Halpern[6], R. S. Hill[5], G. Hinshaw[7], A. Kogut[7], E. Komatsu[8], D. Larson[3], M. Limon[9], S. S. Meyer[10], M. R. Nolta[11], N. Odegard[5], L. Page[2], K. M. Smith[12], D. N. Spergel[12,13], G. S. Tucker[14], J. L. Weiland[5], E. Wollack[7], E. L. Wright[15]

ABSTRACT

New full sky temperature and polarization maps based on seven years of data from *WMAP* are presented. The new results are consistent with previous results, but have improved due to reduced noise from the additional integration time, improved knowledge of the instrument performance, and improved data analysis procedures. The improvements are described in detail.

---

[1] *WMAP* is the result of a partnership between Princeton University and NASA's Goddard Space Flight Center. Scientific guidance is provided by the *WMAP* Science Team.

[2] Dept. of Physics, Jadwin Hall, Princeton University, Princeton, NJ 08544-0708

[3] Dept. of Physics & Astronomy, The Johns Hopkins University, 3400 N. Charles St., Baltimore, MD 21218-2686

[4] Astrophysics, University of Oxford, Keble Road, Oxford, OX1 3RH, UK

[5] ADNET Systems, Inc., 7515 Mission Dr., Suite A100 Lanham, Maryland 20706

[6] Dept. of Physics and Astronomy, University of British Columbia, Vancouver, BC Canada V6T 1Z1

[7] Code 665, NASA/Goddard Space Flight Center, Greenbelt, MD 20771

[8] Univ. of Texas, Austin, Dept. of Astronomy, 2511 Speedway, RLM 15.306, Austin, TX 78712

[9] Columbia Astrophysics Laboratory, 550 W. 120th St., Mail Code 5247, New York, NY 10027-6902

[10] Depts. of Astrophysics and Physics, KICP and EFI, University of Chicago, Chicago, IL 60637

[11] Canadian Institute for Theoretical Astrophysics, 60 St. George St, University of Toronto, Toronto, ON Canada M5S 3H8

[12] Dept. of Astrophysical Sciences, Peyton Hall, Princeton University, Princeton, NJ 08544-1001

[13] Princeton Center for Theoretical Physics, Princeton University, Princeton, NJ 08544

[14] Dept. of Physics, Brown University, 182 Hope St., Providence, RI 02912-1843

[15] UCLA Physics & Astronomy, PO Box 951547, Los Angeles, CA 90095–1547

The seven year data set is well fit by a minimal six-parameter flat ΛCDM model. The parameters for this model, using the *WMAP* data in conjunction with baryon acoustic oscillation data from the Sloan Digital Sky Survey and priors on H_0 from Hubble Space Telescope observations, are: $\Omega_b h^2 = 0.02260 \pm 0.00053$, $\Omega_c h^2 = 0.1123 \pm 0.0035$, $\Omega_\Lambda = 0.728^{+0.015}_{-0.016}$, $n_s = 0.963 \pm 0.012$, $\tau = 0.087 \pm 0.014$ and $\sigma_8 = 0.809 \pm 0.024$ (68 % CL uncertainties).

The temperature power spectrum signal-to-noise ratio per multipole is greater that unity for multipoles $\ell \lesssim 919$, allowing a robust measurement of the third acoustic peak. This measurement results in improved constraints on the matter density, $\Omega_m h^2 = 0.1334^{+0.0056}_{-0.0055}$, and the epoch of matter-radiation equality, $z_{\rm eq} = 3196^{+134}_{-133}$, using *WMAP* data alone.

The new *WMAP* data, when combined with smaller angular scale microwave background anisotropy data, results in a 3σ detection of the abundance of primordial Helium, $Y_{\rm He} = 0.326 \pm 0.075$. When combined with additional external data sets, the *WMAP* data also yield better determinations of the total mass of neutrinos, $\sum m_\nu =< 0.58$ eV (95% CL), and the effective number of neutrino species, $N_{\rm eff} = 4.34^{+0.86}_{-0.88}$. The power-law index of the primordial power spectrum is now determined to be $n_s = 0.963 \pm 0.012$, excluding the Harrison-Zel'dovich-Peebles spectrum by $> 3\sigma$

These new *WMAP* measurements provide important tests of Big Bang cosmology.

Subject headings: cosmic microwave background, space vehicles: instruments

1. Introduction

The Wilkinson Microwave Anisotropy Probe (*WMAP*) is a NASA sponsored satellite designed to map the Cosmic Microwave Background (CMB) radiation over the entire sky in five frequency bands. It was launched in June 2001 from Kennedy Space Flight Center and began surveying the sky from its orbit around the the Earth-Sun L2 point in August 2001. This work and the accompanying papers comprise the fourth in a series of biennial data releases and incorporates seven years of observational data.

Results from the one-year, three-year and five-year results are summarized in Bennett et al. (2003a), Jarosik et al. (2007) and Hinshaw et al. (2009) respectively, and references therein. An overall description of the mission including instrument nomenclature is contained in Bennett et al. (2003b) and Limon et al. (2010), while details of the optical system and radiometers can be found in Page et al. (2003b) and Jarosik et al. (2003).

The primary data product of *WMAP* are sets of calibrated sky maps at five frequency bands centered at 23 GHz (K band), 33 GHz (Ka band), 41 GHz (Q band), 61 GHz (V band) and 94 GHz (W band), including measured noise levels and beam transfer functions that describe the smoothing of the sky signal resulting from the beam geometries. These maps are provided for Stokes I, Q and U parameters on a year by year basis and in a year co-added format, and at several pixel resolutions appropriate for various analyses. Changes relative to the previous data release include the inclusion of seven years of observational data, a new masking procedure that simplifies the map-making process, and improvements of the beam maps and window functions. Details of the processing used to generate these products are described in the remainder of this work.

In an accompanying paper Gold et al. (2010) utilize the maps in the five frequency bands and some external data sets to estimate levels of Galactic emission in each map, and describe the generation of a set of reduced foreground sky maps based on template cleaning, and a map generated using an Internal Linear Combination map (ILC) of *WMAP* data, both of which are used for analysis of the CMB anisotropy signal.

Larson et al. (2010) describe the measurement of the angular power spectrum of the CMB obtained from the reduced foreground sky maps and the cosmological parameters obtained by fitting the CMB power spectra to current cosmological models.

The cosmological implications of the data, including the use of external data sets, are discussed by Komatsu et al. (2010), while Bennett et al. (2010) discuss a number of arguably anomalous results detected in previous *WMAP* data releases.

Weiland et al. (2010) describe the characteristics of a group of point-like objects observed by *WMAP* in the context of their use as microwave calibration sources for astronomical observations.

The remainder of this paper is organized as follows: Section 2 presents updates on the data processing procedures used to generate the seven-year sky maps and related data products. Section 3 describes ongoing efforts to characterize the *WMAP* beam shapes, while Section 4 presents the seven-year sky map data and power spectra, describes some additional analyses on the low-ℓ polarization power spectra, and summarizes the scientific results obtained from the latest *WMAP* data set.

2. Data Processing Updates

2.1. Operations

The sixth and seventh years of *WMAP* 's operation span the interval from 00:00:00 UT, 9 August 2006 (day number 222) to 00:00:00 UT, 10 August 2008 (day number 222) and includes nine short periods when observations were interrupted. These periods include eight scheduled events: six station keeping maneuvers, and one maneuver to avoid flying through the Earth's shadow (11 November 2007), followed by a small orbital correction 19 days later. The other interruption to observations occurred as a result of the failure of the primary transmitter used to telemeter data to Earth. *WMAP* was subsequently reconfigured to use its backup transmitter and normal operations resumed with no performance degradation. On 1 August 2008 (day number 141) *WMAP* flew through the Moon's shadow, causing a $\approx 4\%$ decrease in the incident solar flux lasting ≈ 6h. *WMAP* remained in normal observing mode throughout this event, but data was excluded from sky map processing due to minor instrument thermal perturbations as described in § 2.3.

2.2. Calibration

The algorithm used to calibrate the time ordered data (TOD) is the same as was used for the five-year processing (Hinshaw et al. 2009). Calibration occurs in two steps. First an hourly absolute gain and baseline are determined. The absolute calibration is based on the CMB monopole temperature (Mather et al. 1999) and the velocity dependent dipole resulting from *WMAP* 's orbit about the solar system barycenter. The calibration is performed iteratively, since removing the fixed sky signals arising from the barycentric CMB signal and foregrounds requires values of both the gain and baseline solutions. The only change made to this step of the calibration procedure is that the initial value for the barycentric CMB dipole signal has been updated to agree with the value determined from the five-year analysis.

The second step in the calibration procedure consists of fitting the hourly radiometer gain values to a model which relates the gain to measured values of radiometer parameters. The functional form of the gain model is the same as for the five-year data release, but the fitting procedure now utilizes all seven years of observational data. The seven-year mean changes in the calibration are presented in Table 1. Note that the rms of the fractional calibrations change, $\Delta G/G$, is only 0.05%. The absolute calibration accuracy is estimated to be 0.2%, unchanged from the previously published value.

For K, Ka, and Q bands, there is a small but significant year-to-year variation in the

Table 1. Noise and Calibration Summary for the Template Cleaned and Uncleaned Maps

DA	σ_0(I)	σ_0(Q, U)	σ_0(Q, U)	$\Delta G/G$ [a]
	uncleaned		template cleaned [b]	
	(mK)	(mK)	(mK)	(%)
K1	1.437	1.456	NA	-0.14
Ka1	1.470	1.490	2.192	-0.01
Q1	2.254	2.280	2.741	0.01
Q2	2.140	2.164	2.602	0.01
V1	3.319	3.348	3.567	-0.03
V2	2.955	2.979	3.174	-0.03
W1	5.906	5.940	6.195	-0.05
W2	6.572	6.612	6.896	-0.04
W3	6.941	6.983	7.283	-0.08
W4	6.778	6.840	7.134	-0.12

[a] $\Delta G/G$ is the change in calibration of the current (seven-year) processing relative to the five-year processing. A positive value means that features in the seven-year maps are larger than the same features in the five-year map.

[b] The σ_0 value for the Stokes I template cleaned maps is the same as for the uncleaned maps.

WMAP calibration that can be seen as variations of the Galactic plane brightness in yearly sky maps. This has been measured by correlating each yearly map against the 7-year map for pixels at $|b| < 10°$. A slope and offset is fit to each correlation and the slope values are adopted as yearly calibration variations. These are shown in Figure 1 and are consistent with the 0.2% absolute calibration uncertainty.

2.3. Gaps in Observations

The *WMAP* instrument provides the highest quality data when the observatory is scanning the sky in its nominal observing mode and the instrument thermal environment is stable. Periodically, conditions arise that result in one or both of these conditions not being met. These situations arise from scheduled station-keeping maneuvers, and unscheduled events, such as solar flares or on-board equipment malfunctions. Data taken during these periods are excluded from the sky map processing to ensure the highest quality data products. Previously, potentially corrupted data segments were identified by manually inspecting the event logs and instrument thermal trend plots. The current data release uses a more objective automated procedure to identify the unusable data segments. The automated procedure was designed to approximate the manual procedure, but small differences will occur in the sky coverage between the first five years of the current data release and the previous five-year data release. Using the new procedure *WMAP* still achieves an overall observing efficiency of $\approx 98.4\%$, down slightly from its previous value of $\approx 99\%$.

The automated procedure identifies suspect events based on the time-derivative of the focal plane assembly (FPA) temperature. The measured FPA temperature is averaged over one hour intervals, and the time derivative is formed by differencing successive values of these averages. Suspect thermal events are delineated by the times at which the magnitude of this derivative initially exceeds then finally falls below a threshold value. The threshold has been chosen to be 5 times the rms deviation of the temperature derivative signal occurring during normal observing periods, and corresponds to a value of ≈ 0.75 mK h^{-1}. In situations where the observatory was taken out of normal observing mode (e.g., during a scheduled station keeping maneuver) the duration of the event is lengthened if needed to encompass the entire time the observatory was not in normal observing mode. For each event data from 1.2 hours before the event began to 7.25 hours after the event ended is excluded from sky map processing.

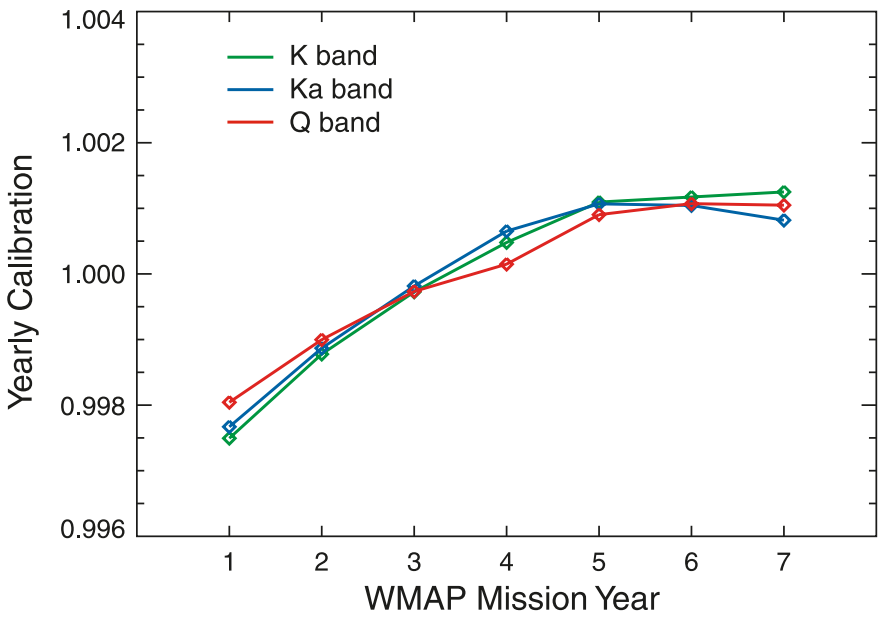

Fig. 1.— Measurements of the year-to-year calibration variation for K, Ka and Q bands obtained by correlating the Galactic plane signal in the seven-year map to the signal in single year sky maps. Note that the measured variations are consistent with the estimated absolute calibration uncertainty of 0.2%. No significant variation is seen for the V and W band maps.

2.4. Planet Masking

In the one, three and five-year data analyses, observations when the boresight of each telescope beam fell within 1°.5 of Mars, Jupiter, Saturn, Uranus or Neptune were excluded from sky map processing, preventing contamination of the sky maps by emission from the planets. Subsequent analysis has shown that even with these exclusion criteria microwave emission from Jupiter could generate as much as a 75 μK (in K band) errant signal in a narrow annulus surrounding the region of excluded observations. Although there is no indication that this influenced the cosmological analysis, the radii used to exclude observations have been increased for the seven-year analysis, chosen to limit planetary leakage to less than 1 μK. However, given the uncertainty in the determination of the beam profiles at these levels, we adopt a conservative upper bound on possible planetary signal leakage into the TOD used for sky map production of 5 μK. The new values are displayed in Table 2.

2.5. Expanded Diffuse Galactic Foreground Mask

The mask for diffuse Galactic emission has been revised by including areas near the plane where the diffuse foreground cleaning algorithm appears to be less efficient than for the sky at large. These areas are found by performing a pixel-by-pixel χ^2 test comparing null maps to cleaned Q-V and V-W maps with resolution degraded from r9 [1] to r5. All pixels with χ^2 greater than 4 times that of the χ^2 in the polar caps regions are cut. Small islands of cut pixels are eliminated from the cut if they contain 4 or fewer contiguous pixels. The two

[1] *WMAP* uses the HEALPix (Gorski et al. 2005) pixelization and labels resolution as r4, r5, r9 and r10 corresponding to HEALPix $N_{\rm side}$ values of 16, 32, 512 and 1024 respectively.

Table 2. Data Exclusion Radii for the Planets

	Frequency Band				
Planet	K	Ka	Q	V	W
Mars	2°.0	1°.5	1°.5	1°.5	1°.5
Jupiter	3°.0	2°.5	2°.5	2°.2	2°.0
Saturn	2°.0	1°.5	1°.5	1°.5	1°.5
Uranus	2°.0	1°.5	1°.5	1°.5	1°.5
Neptune	2°.0	1°.5	1°.5	1°.5	1°.5

resulting masks based on Q-V and V-W analyses, respectively, are combined and promoted back to r9. The edges of the cut are smoothed by convolving the mask with a Gaussian of 3° FWHM and cutting the result at a value of 0.5. As the final step, the smoothed cut is combined with the five-year *KQ85* or *KQ75* cut (Gold et al. 2010). The resulting masks, termed *KQ85y7* and *KQ75y7*, admit 78.3% and 70.6% of the sky, respectively, as compared to 81.7% and 71.6% for the five-year versions—a decrease of the admitted sky area by 3.4% of the full sky for *KQ85* and 1.0% for *KQ75*.

2.6. Map-Making with Asymmetric Masking

The most significant change in the current processing is the use of asymmetric masking in the iterative reconstruction of the sky maps. *WMAP* 's differential design means that the time-ordered-data (TOD) represents differences between the intensities of pairs of points on the sky observed by the two telescope beams. Reconstructing sky maps from differential data requires solving a set of linear equations that describe the relation between the differential TOD and the sky signal. Solution of this set of equations is performed iteratively, using sky maps from earlier iterations to alternately remove estimated sky signals for each beam from the TOD, leaving the value associated with the opposite beam which is then used to generate the next iteration of the sky map. This procedure becomes problematic when one of the beams is in a region of high intensity and the other is in a region of low intensity. Small errors arising from pixelization, residual pointing errors, beam ellipticity or radiometer gain errors limit the degree to which the signal associated with the beam in the high emission region can be estimated. Such errors result in errant signals being introduced into sky map pixels associated with the beam in the low intensity region. This potential problem is circumvented by masking portions of the data when such errors are likely to be introduced.

In the *WMAP* first year results an asymmetric masking procedure was used (Hinshaw et al. 2003). Asymmetric masking means that when one beam is in a high Galactic emission region (as determined by a processing mask (Limon et al. 2010)) and the other beam is in a low Galactic emission region, only the pixel in the high emission region is iteratively updated. This allows for the reconstruction of full sky maps while avoiding the situation that could produce an errant signal. The maps, $\mathbf{t}_1$, were obtained through a simple iterative solution of the linear equation

$$\mathbf{t}_1 = \mathbf{W}\mathbf{d}_1 \tag{1}$$

where $\mathbf{d}_1$ is the pre-whitened time ordered data and $\mathbf{W} = (\mathbf{M}^T\mathbf{M})^{-1} \cdot \mathbf{M}^T$. The matrix $\mathbf{M}$ is the mapping function, which has N_p columns and N_t rows, corresponding to the number of sky map pixels and time-ordered data points respectively. When the map processing includes

polarization degrees of freedom N_p is four times the number of map pixels, corresponding to the Stokes I, Q and U components and a spurious component, S, used to absorb effects arising from bandpass differences between the two radiometers comprising each differencing assembly (DA). See Jarosik et al. (2007) for a description of the implementation of the spurious mode, S. Multiplying a sky map vector by $\mathbf{M}$ effectively generates the time ordered data that would be obtained if *WMAP* observed a sky corresponding to the map vector. The sky maps obtained by solving equation 1 are an unbiased representation of the true sky signal, but do not treat the noise terms optimally.

The *WMAP* three-year (Jarosik et al. 2007) and five-year (Hinshaw et al. 2009) analyses generated maximum likelihood map solutions using a conjugate gradient iterative technique. The maximum likelihood estimate of the sky map, $\tilde{\mathbf{t}}$, is

$$\tilde{\mathbf{t}} = (\mathbf{M}^T\mathbf{N}^{-1}\mathbf{M})^{-1} \cdot (\mathbf{M}^T\mathbf{N}^{-1}\mathbf{d}) \tag{2}$$

where $\mathbf{d}$ is the calibrated but unfiltered time ordered data, and $\mathbf{N}^{-1}$ is the inverse of the radiometer noise covariance matrix. Solution of this equation involves a direct evaluation of the last term of equation 2 once, resulting in a map $\mathbf{t_0} = \mathbf{M}^T\mathbf{N}^{-1}\mathbf{d}$, followed by the iterative solution of the equation

$$\tilde{\mathbf{t}} = (\mathbf{M}^T\mathbf{N}^{-1}\mathbf{M})^{-1} \cdot \mathbf{t_0}. \tag{3}$$

Solving this equation with the conjugate gradient method requires the use of symmetric masking since this method can only be used when the matrix multiplying $\mathbf{t_0}$ (in this case $(\mathbf{M}^T\mathbf{N}^{-1}\mathbf{M})^{-1}$) is symmetric . Symmetric masking means that if either beam is in a region of high Galactic emission, neither pixel is updated. Symmetric masking is implemented by simply replacing all occurrences of the full sky mapping matrix, $\mathbf{M}$, with a masked version of the matrix in equations (2 and 3). Since symmetric masking produces sky maps with no information in the high Galactic emission regions, in previous analyses two sets of sky maps were generated, symmetrically masked maps, and full sky maps incorporating no masking. Data from full sky maps were used to fill in regions of the symmetrically masked maps which contained no data. This procedure was a significant advancement over the iterative procedure used in the *WMAP* first year results, in that it produced maximum likelihood maps and allowed for direct determination of the level of convergence of the solution. Its major disadvantages are that two sets of maps have to be generated then pieced together, and there is no simple method of calculating a pixel-pixel noise matrix which describes the noise covariance between pixels obtained from the two different input maps. The pixel-pixel noise covariance matrix delivered with the data release only applied to the pixels in the low-Galactic emission regions, and only diagonal weights are used to describe the noise properties in the regions of high Galactic emission.

Incorporating asymmetric masking into the maximum likelihood sky maps solution requires solving the equation

$$\tilde{\mathbf{t}} = (\mathbf{M}_{\rm am}^{\mathbf{T}}\mathbf{N}^{-1}\mathbf{M})^{-1} \cdot (\mathbf{M}_{\rm am}^{\mathbf{T}}\mathbf{N}^{-1}\mathbf{d}) \tag{4}$$

where $\mathbf{M}_{\rm am}^{T}$ is the mapping matrix incorporating asymmetric masking and $\mathbf{M}$ is the unmasked mapping matrix. Again, this equation is solved by direct evaluation of the last term,

$$\mathbf{t}_0 = \mathbf{M}_{\rm am}^{\mathbf{T}}\mathbf{N}^{-1}\mathbf{d} \tag{5}$$

once, followed by an iterative solution of the equation

$$\tilde{\mathbf{t}} = (\mathbf{M}_{\rm am}^{T}\mathbf{N}^{-1}\mathbf{M})^{-1} \cdot \mathbf{t_0}. \tag{6}$$

Note that the matrix $\mathbf{M}_{\rm am}^{T}\mathbf{N}^{-1}\mathbf{M}$ is not symmetric, and therefore this equation cannot be solved using a simple conjugate gradient algorithm as was done previously. A bi-conjugate gradient stabilized method (Barrett et al. 1994) was chosen to solve this equation since it offered good convergence properties and was straightforward to implement, requiring relatively minor changes to the existing procedures. This technique was verified by reconstructing input maps to numerical precision from simulated noise-free TOD. Utilizing asymmetric masking eliminates both of the aforementioned shortcomings of the simple conjugate gradient method - each DA only requires a single map solution, and a pixel-pixel inverse noise covariance matrix can be generated which describes the noise correlation between all the pixels in the map.

2.7. Calculation of the pixel-pixel noise covariance matrix, $\mathbf{\Sigma}$

The pixel-pixel noise covariance matrix is given by $\mathbf{\Sigma} = \langle \tilde{\mathbf{t}}_{\rm n}\tilde{\mathbf{t}}_{\rm n}^{T}\rangle$, where $\mathbf{t_n}$ is the noise component of a reconstructed sky map and the brackets denote an ensemble average. The time-ordered data, $\mathbf{d}$, used to generate the map may be written as the sum of a signal term and a noise term

$$\mathbf{d} = \mathbf{M}\mathbf{t} + \mathbf{n} \tag{7}$$

where $\mathbf{M}$ is the full sky (unmasked) mapping matrix, $\mathbf{t}$ is a vector representing the input sky signal and $\mathbf{n}$ is a vector corresponding to the radiometer noise, its covariance being described as

$$\mathbf{N} = \langle \mathbf{n}\mathbf{n}^{\rm T}\rangle. \tag{8}$$

The noise component of the maximum likelihood asymmetrically masked map solution may be written as

$$\tilde{\mathbf{t}}_{\rm n} = (\mathbf{M}_{\rm am}^{\mathbf{T}}\mathbf{N}^{-1}\mathbf{M})^{-1} \cdot (\mathbf{M}_{\rm am}^{\mathbf{T}}\mathbf{N}^{-1}\mathbf{n}). \tag{9}$$

The noise covariance matrix becomes

$$\begin{aligned}
\mathbf{\Sigma} &= \langle(\mathbf{M}_{\rm am}^T\mathbf{N}^{-1}\mathbf{M})^{-1}(\mathbf{M}_{\rm am}^T\mathbf{N}^{-1}\mathbf{n})\cdot[(\mathbf{M}_{\rm am}^T\mathbf{N}^{-1}\mathbf{M})^{-1}(\mathbf{M}_{\rm am}^T\mathbf{N}^{-1}\mathbf{n})]^T\rangle && (10)\\
&= \langle(\mathbf{M}_{\rm am}^T\mathbf{N}^{-1}\mathbf{M})^{-1}(\mathbf{M}_{\rm am}^T\mathbf{N}^{-1}\mathbf{n})\cdot(\mathbf{n}^T\mathbf{N}^{-1}\mathbf{M}_{\rm am})(\mathbf{M}^T\mathbf{N}^{-1}\mathbf{M}_{\rm am})^{-1}\rangle && (11)\\
&= (\mathbf{M}_{\rm am}^T\mathbf{N}^{-1}\mathbf{M})^{-1}(\mathbf{M}_{\rm am}^T\mathbf{N}^{-1})\cdot(\langle\mathbf{n}\mathbf{n}^T\rangle\mathbf{N}^{-1})\mathbf{M}_{\rm am}(\mathbf{M}^T\mathbf{N}^{-1}\mathbf{M}_{\rm am})^{-1} && (12)\\
&= (\mathbf{M}_{\rm am}^T\mathbf{N}^{-1}\mathbf{M})^{-1}\cdot(\mathbf{M}_{\rm am}^T\mathbf{N}^{-1}\mathbf{M}_{\rm am})\cdot(\mathbf{M}^T\mathbf{N}^{-1}\mathbf{M}_{\rm am})^{-1}. && (13)
\end{aligned}$$

In practice the terms $\mathbf{M}_{\rm am}^T\mathbf{N}^{-1}\mathbf{M}$ and $\mathbf{M}_{\rm am}^T\mathbf{N}^{-1}\mathbf{M}_{\rm am}$ are evaluated at r4 with the $\mathbf{N}^{-1}$ normalized to unity at zero lag, and the inverse pixel-pixel noise covariance matrix is generated by forming the product

$$\mathbf{\Sigma}^{-1} = (\mathbf{M}^T\mathbf{N}^{-1}\mathbf{M}_{\rm am})\cdot(\mathbf{M}_{\rm am}^T\mathbf{N}^{-1}\mathbf{M}_{\rm am})^{-1}\cdot(\mathbf{M}_{\rm am}^T\mathbf{N}^{-1}\mathbf{M}). \qquad (14)$$

Regions of the $\mathbf{\Sigma}^{-1}$ matrix corresponding to combinations of Stokes I, Q and U are then converted to noise units by dividing by the appropriate combinations of $\sigma_0(I)$ and $\sigma_0(Q,U)$ given in Table 1.

The term $\mathbf{M}_{\rm am}^T\mathbf{N}^{-1}\mathbf{M}_{\rm am}$ is numerically inverted and is used as the source for the off-diagonal terms of the preconditioner for the bi-conjugate gradient stabilized algorithm.

2.8. $N_{\rm obs}$ Fields of the Maps

The asymmetric masking used to generate sky maps requires a new procedure for calculating the effective number of observations, $N_{\rm obs}$, for each map pixel. In previous data releases the effective number of observations was calculated by accumulating the number of time ordered data points falling within each pixel, weighted by the appropriate transmission imbalance coefficients, $x_{\rm im}$, and polarization projection factors ($\sin 2\gamma$, $\cos 2\gamma$). These values corresponded to the diagonal elements of the inverse pixel-pixel noise covariance matrix $\mathbf{\Sigma}^{-1} = \mathbf{M}^T\mathbf{N}^{-1}\mathbf{M}$ (Jarosik et al. (2007) equation (26)), evaluated assuming white radiometer noise, i.e. $\mathbf{N}^{-1} = \mathbf{I}$. The simple procedure for evaluating these terms is not applicable to the form of $\mathbf{\Sigma}^{-1}$ for the asymmetrically masked maps, equation (14). The $N_{\rm obs}$ fields of the r9 and r10 sky maps were generated by evaluating the diagonal elements of equation (14) with $\mathbf{N}^{-1} = \mathbf{I}$ using sparse matrix techniques. The $N_{\rm obs}$ fields of the r4 sky maps are described in § 2.10.

2.9. Projecting Transmission Imbalance Modes from the $\mathbf{\Sigma}^{-1}$ Matrices

As described in Jarosik et al. (2007), errors in the determination of the transmission imbalance parameters, $x_{\rm im}$, are a potential source of systematic artifacts in the reconstructed

sky maps. These time independent parameters, which specify the difference between the transmission between the A-side and B-side optical systems for each radiometer, are measured from the flight data, and are presented in Table 3. To prevent biasing the cosmological analyses, sky map modes that can be excited by these measurement errors are identified and projected from the Σ^{-1} matrices.

The procedure follows the same method as used in the three and five years analyses and consists of generating a one-year span of simulated time ordered data using the nominal values of the loss imbalance parameters. Sky maps are processed from this archive using the input values of $x_{\rm im}$ and altered values to simulate errors in the measured values of the coefficients. The differences between the resultant maps are used to identify map modes resulting from processing the data with altered $x_{\rm im}$ values. Two modifications have been made to this procedure relative to the previous analyses: (1) The simulated sky maps are formed at r4 by direct evaluation of equations (5, 6) at r4. This change was adopted to eliminate contamination of the transmission imbalance templates by the poorly measured sky map modes associated with monopoles in the Stokes I and spurious mode S sky maps. It was found that varying the $x_{\rm im}$ factors produced large changes in the amplitudes of these poorly measured modes in addition to exciting the mode associated with the loss imbalance. Through utilization of a singular value decomposition it was possible to null the poorly measured modes associated with the aforementioned monopoles while preserving the modes associated with the transmission imbalance while evaluating equation (6). (2) Transmission imbalance modes were evaluated both for the case when the $x_{\rm im}$ for both radiometers comprising each DA were increased 20% above their measured values, and for the case when the $x_{\rm im}$ value for radiometer 1 was increased by 10% and that of radiometer 2 decreased by 10%. (Previously the only combination used was that in which both $x_{\rm im}$ values were increased.) For six of the DAs very similar sky map modes were generated by both sets of $x_{\rm im}$, while for the V2, W1, W2, and W4 somewhat different modes were generated for the two different sets. As a result, only one mode was projected from the K1, Ka1, Q1, Q2, and W3 matrices while two modes were projected out of the the V2, W1, W2 and W4 matrices. In each case the modes were removed from $\mathbf{\Sigma^{-1}}$following the method described in Jarosik et al. (2007).

2.10. Low Resolution Single Year Map Generation

The low resolution sky maps were generated by performing an inverse noise weighted degradation of the high resolution maps that takes into account the intra-pixel noise correlations of the high resolution input maps . The weight matrix for the polarization (Stokes

Q and U) and spurious mode (S) of each high resolution map pixel, p9, is given by

$$\mathbf{N}_{\rm obs}({\rm p9}) = \begin{pmatrix} N_{\rm QQ} & N_{\rm QU} & N_{\rm QS} \\ N_{\rm QU} & N_{\rm UU} & N_{\rm SU} \\ N_{\rm QS} & N_{\rm SU} & N_{\rm SS} \end{pmatrix}, \tag{15}$$

where each element $N_{\rm XY}$ is an element of $\mathbf{\Sigma}^{-1}$ (equation 14) evaluated as described in § 2.8. For each DA year combination the Q, U, S map sets were generated as

$$\begin{pmatrix} Q_{\rm p4} \\ U_{\rm p4} \\ S_{\rm p4} \end{pmatrix} = \left(\mathbf{N}^{\rm tot}_{\rm obs}({\rm p4})\right)^{-1} \sum_{\rm p9 \in p4} \mathbf{N}_{\rm obs}({\rm p9}) \begin{pmatrix} Q_{\rm p9} \\ U_{\rm p9} \\ S_{\rm p9} \end{pmatrix}, \tag{16}$$

$$\mathbf{N}^{\rm tot}_{\rm obs}({\rm p4}) = \sum_{{\rm p9} \in p4} \mathbf{N}_{\rm obs}({\rm p9}). \tag{17}$$

The $N_{\rm obs}$ fields of the low resolution sky maps contain the diagonal elements of the corresponding portions of the $\mathbf{\Sigma}^{-1}$ matrices as described in § 2.7 before the scaling by σ_0 is applied.

2.11. Low Resolution Multi-year Map Generation

The single year single DA maps were combined to form a seven-year map for each DA and seven-year maps for each frequency band. The individual low resolution maps were inverse noise weighted using the $\tilde{\mathbf{\Sigma}}$ matrices (§ 2.9), scaled to reflect the noise level of each DA. The weighted polarization maps were formed as

$$\begin{pmatrix} Q \\ U \end{pmatrix} = \tilde{\mathbf{\Sigma}}^{\rm tot} \sum_{\rm yr,DA} \tilde{\mathbf{\Sigma}}^{\mathbf{-1}}_{\rm yr,DA} \begin{pmatrix} Q \\ U \end{pmatrix}_{\rm yr,DA}, \tag{18}$$

$$\tilde{\mathbf{\Sigma}}^{\rm tot} = \left(\sum_{\rm yr,DA} \tilde{\mathbf{\Sigma}}^{\mathbf{-1}}_{\rm yr,DA} \right)^{-}, \tag{19}$$

where $()^{-}$ represents a pseudo-inverse of the sum in parenthesis. This summation is performed over the year/DA combinations to be included in the final map. For K and Ka-bands the pseudo-inverse is calculated by performing a singular value decomposition of the sum of the $QU \times QU$ $\tilde{\mathbf{\Sigma}}^{\mathbf{-1}}$ matrices and inverting all its eigenvalues except for the smallest, which is set to zero. This procedure de-weights the one nearly singular mode associated with the monopoles in the I and S maps. No modes are removed from the Q, V and W-band maps.

3. Beam Maps and Window Functions

The seven-year *WMAP* beams and window functions result from a refinement of the data reduction methods used for the five-year beams, with no major changes in the processing steps.

Briefly, in the five-year analysis, the beam maps were accumulated from TOD samples with Jupiter in either the A or the B side beam. Sky background was subtracted using the seven-year full-sky maps, with the band dependent Jupiter exclusion radii (§2.4). Because of the motion of Jupiter, and the numerous Jupiter observing seasons[2], the sky coverage of the maps was 100% in spite of this masking.

As far as possible, the beam transfer functions b_ℓ in Fourier space were computed directly from Jupiter data. However, at low signal levels, some information was incorporated from beam models. The A and B side Jupiter data were fitted separately by a physical optics model comprising feed horns with fixed profiles, together with primary and secondary mirrors described by fit parameters. The geometrical configuration of these components was fixed. The fitted parameters described small distortions of the mirror surface shapes.

The beam models were combined with the Jupiter data at low signal levels by a hybridization algorithm. This process was optimized to yield the minimum uncertainty in beam solid angle, given the instrumental noise, under the conservative assumption that the systematic error in the beam model was 100%. Details, as well as a summary of beam processing in earlier data releases, were given by Hill et al. (2009).

In addition to the use of three more seasons of Jupiter data, the following refinements, described below in more detail, have been made for the seven-year beam processing:

- Subtraction of background flux from Jupiter observations is improved by expanding the exclusion radius for sky maps (§ 2.4)
- The beam modeling procedure was modified by adding additional terms to the description of the secondary mirror figure to approximate a hypothetical tip/tilt.
- The rate of convergence of the physical optics models is improved by correcting an orthogonalization error in the conjugate gradient code.
- The physical optics fit is driven harder in two senses:

[2]A "season" is a ≈ 45 day period when a planet falls within the scan pattern of *WMAP* . Each planet typically has two seasons per year.

1. A smaller change in χ^2 between conjugate gradient descent steps is required to declare convergence.
2. The model is fitted over a wider field of view in the observed beam map.

The change in beam profiles and transfer functions between the five- and seven-year analyses is conveniently summarized by a comparison of solid angles for the 10 DAs, given in Table 4. The solid angle increases of 0.8% in K1 and 0.4% in Ka1 are the result of the improved background estimates for the Jupiter observations. The solid angle changes for the Q1–W4 DAs have multiple causes. First, the instrumental noise in the Jupiter samples is different in detail. Second, the beam models have been refitted and differ slightly from the five-year versions. Third, the increased S/N of the Jupiter data in the beam wings means that for some DAs, the hybrid threshold is optimized to a lower gain with 7 years of data. This value is the limit below which observed intensity values in the Jupiter TOD are replaced with computed values from the beam model. For the 5 year data analysis, the hybrid thresholds were 3, 4, 6, 8, and 11 dBi, respectively, for bands K, Ka, Q, V, and W (Hill et al. 2009). For the seven-year data analysis, the V and W thresholds are 7 and 10 dBi, respectively, while those for K, Ka, and Q are unchanged.

As shown in the table, the aggregate solid angle changes for V and W, which are the bands used in the high-ℓ TT power spectrum, are $\sim 0.1\%$ or less. Table 4 also gives the current values of the forward gain G_m and of the factor $\Gamma_{\rm ff}$ for converting antenna temperature to flux in Jy. New hybrid beam profiles and beam transfer functions b_ℓ are available online from the Legacy Archive for Microwave Background Data Analysis (LAMBDA).

3.1. Seven-year Beam Model Fitting

3.1.1. Secondary Tip/Tilt

One change in the seven-year beam computations is to introduce approximate tip/tilt terms for the secondary mirror into the physical optics model. This change is motivated by the stable $\sim 0\overset{\circ}{.}1$ offset in the collective B-side boresight pointings, as compared to pre-flight expectations (Hill et al. 2009). In previous beam fits, this offset was absorbed by two free-floating nuisance parameters.

The introduction of secondary tip/tilt is a heuristic attempt to improve the fidelity of the beam model. Because a displacement in beam pointings could result from various small mechanical displacements in the instrument, or from a combination of them, the beams contain too little information to support a mechanical analysis. We emphasize that the

boresight pointings on both the A and the B sides are equally stable since launch, to $< 10''$ (Jarosik et al. 2007), an estimate that is confirmed by the full seven-year Jupiter data.

For convenience, we approximate tip/tilt as a purely planar surface distortion of the secondary mirror, in addition to the Bessel modes used previously. The pivot line is allowed to vary by including a term for scalar displacement together with tip/tilt slopes in two orthogonal directions.

This parameter subspace has been explored using Monte Carlo beam simulations, which reveal a strong degeneracy between the scalar offset and a tilt in the spacecraft YZ plane, because both displacements move the illumination spot on the primary mirror in the up or down direction. Therefore, we have investigated a family of solutions by adopting an *Ansatz* for the mechanical constraints, such that (1) one edge of the secondary is allowed to pivot while pinned at the designed position, (2) the opposite edge undergoes a small displacement, and (3) the secondary mirror as a whole is rigid.

These constraints result in two discrete solutions for each secondary mirror; for each side of the instrument, the solution requiring the smaller mechanical displacement is chosen. The resulting edge displacement is -4.4 mm on the B side, which corresponds to a hypothetical motion of one edge of the secondary mirror away from the secondary backing structure and toward the primary. Similarly, this method results in a hypothetical displacement of one edge of the A-side secondary by 0.2 mm away from the primary. However, as already explained, this mechanical interpretation is uncertain. For subsequent stages of beam modeling, the distortion coefficients mimicking tip/tilt and displacement of the secondary mirrors are held fixed.

3.1.2. Fitting Process

The overall fitting of beams progresses much as it did for the five-year data. On each of the A and B sides, the primary mirror is modeled with Fourier modes added to the nominal mirror figure. Similarly, the secondary mirror is modeled with Bessel modes. A complete fit is done using modes with spatial frequency on the mirror surface up to some maximum value. When convergence is achieved, the current best-fit parameters become the starting point for a new fit with a higher spatial frequency limit. The primary mirror spatial frequencies are indexed using an integer k, such that the wavelength of the mirror surface distortion is 280 cm/k. The secondary modes are specified by the Bessel mode indexes n and k. Details are given in Hill et al. (2009), §2.2.2. The maximum spatial frequencies fitted are defined by $k_{\max} = 24$ on the primary and $n_{\max} = 2$ on the secondary.

Because the Fourier modes are non-orthogonal over the circular domain of the primary mirror distortions, the fitting is actually done in an orthogonalized space (Hill et al. 2009). A bug in the orthogonalization code was corrected before the seven-year analysis began; this bug only affected speed of convergence, not the definition of χ^2, so the five-year results remain valid. However, this change made it practical to refit the beam models *ab initio* from the nominal mirror figures, i.e., with zero for all Fourier and Bessel coefficients, rather than beginning from the five-year solution.

The χ^2 changes from the five-year to the seven-year beam models are shown in Table 5. The χ^2 values shown for the five-year models are recomputed using seven-year data. It is clear from Table 5 that the overall improvement in the model for the 10 DAs collectively is driven primarily by the W band on the A side and the V and W bands on the B side.

Figure 2 shows model beam profiles from an example DA, W1, from both the five-year and the seven-year analyses. The A-side model has a similar profile in the five-year and seven-year fits, with small trade-offs in fit quality at various radii. However, the B-side model shows a new feature in the seven-year fitting, namely, an elevated response at large radii and very low signal levels in the V and W bands. This feature is seen at radii larger than 2° in the right-hand panel of Figure 2, where the seven-year profile (red) is very slightly higher than the five-year profile (blue). The five-year and seven-year profiles for the example DA differ by a factor of $\sim 2 - 10$ in this region, although both are $\gtrsim 50$ dB down from the beam peak.

Several attempts have been made using jumps in the fitting parameters (as in simulated annealing) to find a region of parameter space in the A-side fit that would lead to the existence of elevated tails similar to those on the B side. So far, such attempts have failed. The best A-side fit lacks the elevated-tail feature, while the best B-side fit has it.

Just as in the five-year analysis, none of the beam models meets a formal criterion for a good fit, since the number of degrees of freedom is of order 10^5, or 10^4 per DA, while the overall χ^2_ν is ~ 1.05. However, the model beams are used only in a restricted role, more than ~ 45 dB below the beam peak, so that the primary contribution to the beams and b_ℓ is directly from Jupiter data. As a result, the effect of any particular feature of the models is either omitted or diluted in the final result. However, the B-side model tail mentioned above increases the beam uncertainty slightly at large radii as compared to the five-year analysis.

The process for incorporating information from the models into the Jupiter-based beams is explained by Hill et al. (2009). This process is termed *hybridization*. Briefly, the beam profiles are integrated from Jupiter TOD. The two-dimensional coordinates of each TOD point within the beam model are determined. If the model gain is below a certain threshold, then

the model gain is substituted for the Jupiter measurement. The thresholds are optimized for each DA by minimizing the uncertainty in the solid angle, under the assumption that the beam model is subject to a scaling uncertainty of 100%. Final hybrid profiles combining the A and B sides are shown for the W1 DA, for both the five-year and the seven-year analysis, in Figure 3.

The beam transfer function, b_ℓ, is integrated directly from the hybrid beam profiles, and the error envelope for b_ℓ is computed using a Monte Carlo method. These procedures are the same as in the five-year analysis (Hill et al. 2009). A comparison of five-year and seven-year b_ℓ and the corresponding uncertainties is shown in Figure 4.

3.2. Flux Conversion Factors and Beam Solid Angles for Point Sources

The conversion factor from peak antenna temperature to flux density for a point source is given by (Page et al. 2003a)

$$\Gamma = c2/2k_B\Omega_{eff}(\nu_{eff})^2 \tag{20}$$

where Ω_{eff} is the effective beam solid angle of the A and B sides combined and ν_{eff} is the effective band center frequency, both of which depend on the source spectrum. New values of these quantities have been calculated that supersede previous results given for point sources.

For a point source with antenna temperature spectrum $T_A \propto \nu^\beta$, the effective frequency is determined from

$$\nu_{eff}^\beta = \int f(\nu)G_m(\nu)\nu^\beta d\nu / \int f(\nu)G_m(\nu)d\nu \tag{21}$$

where $f(\nu)$ is the passband response, and $G_m(\nu)$ is the forward gain. This is consistent with the definition used by Jarosik et al. (2003) for a beam-filling source, except in that case the forward gain is not included. Values of $\nu_{eff}(\beta)$ are calculated using pre-flight bandpass measurements and pre-flight GEMAC[3] measurements of forward gain. A correction for scattering is applied to the GEMAC measurements,

$$G_m(\nu) = G_m^{GEMAC}(\nu)e^{(-(4\pi\sigma/\lambda)^2)} \tag{22}$$

where σ is an effective rms primary mirror deformation whose value is set separately for each DA based on the degree of scattering estimated from the pass 4 physical optics modeling.

[3]Goddard Electromagnetic Anechoic Chamber

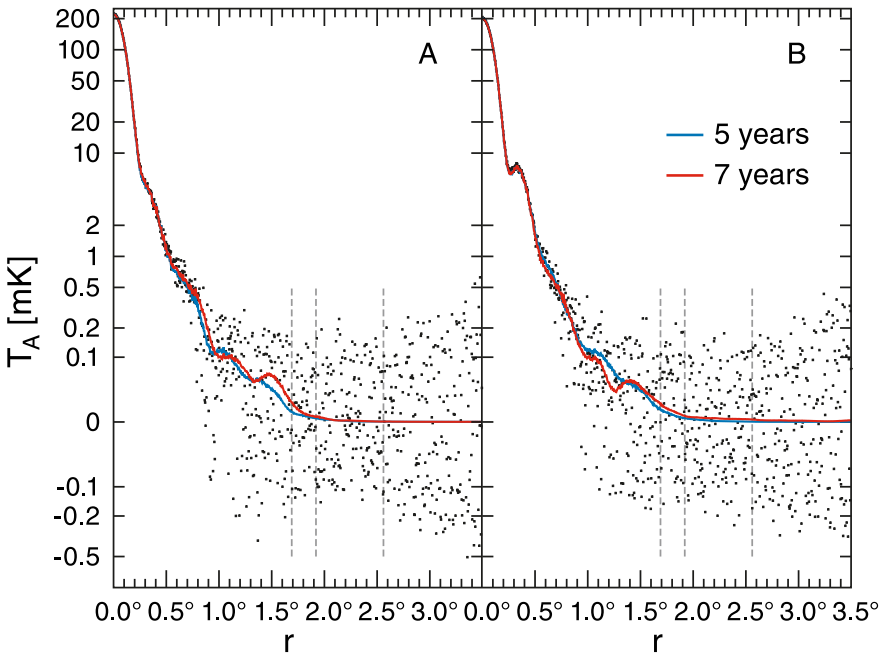

Fig. 2.— Physical optics beam models for the W1 DA on the A side (left) and B side (right) of the *WMAP* instrument. The ordinate is scaled by a $\sinh^{-1}$ function that provides a smooth transition between linear and logarithmic regimes. *Blue*: five-year models; *red*: seven-year models. *Points*: seven-year Jupiter beam data averaged in radial bins of $\Delta r = 0\overset{\prime}{.}5$. *Dashed lines*: Radii at which hybrid beam profiles consist of 90%, 50%, and 10% Jupiter data, respectively, from smaller to larger radii. Model differences inside $r \sim 1\overset{\circ}{.}7$ are mostly suppressed in the hybrid beam profiles, whereas model differences outside $r \sim 2\overset{\circ}{.}6$ are mostly retained.

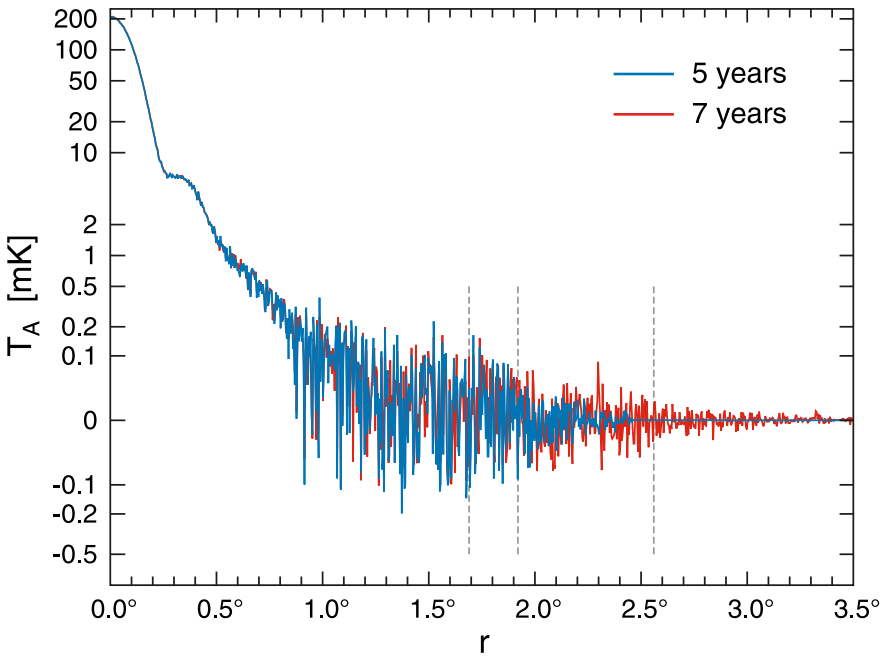

Fig. 3.— W1 hybrid beam profiles from five-year (blue) and seven-year (red) analysis, combined for the A and B sides. The ordinate is scaled by a $\sinh^{-1}$ function that provides a smooth transition between linear and logarithmic regimes. *Dashed lines*: Radii at which hybrid beam profiles consist of 90%, 50%, and 10% Jupiter data, respectively, from smaller to larger radii. The noise shows that use of Jupiter data extends effectively to larger radii in the seven-year analysis.

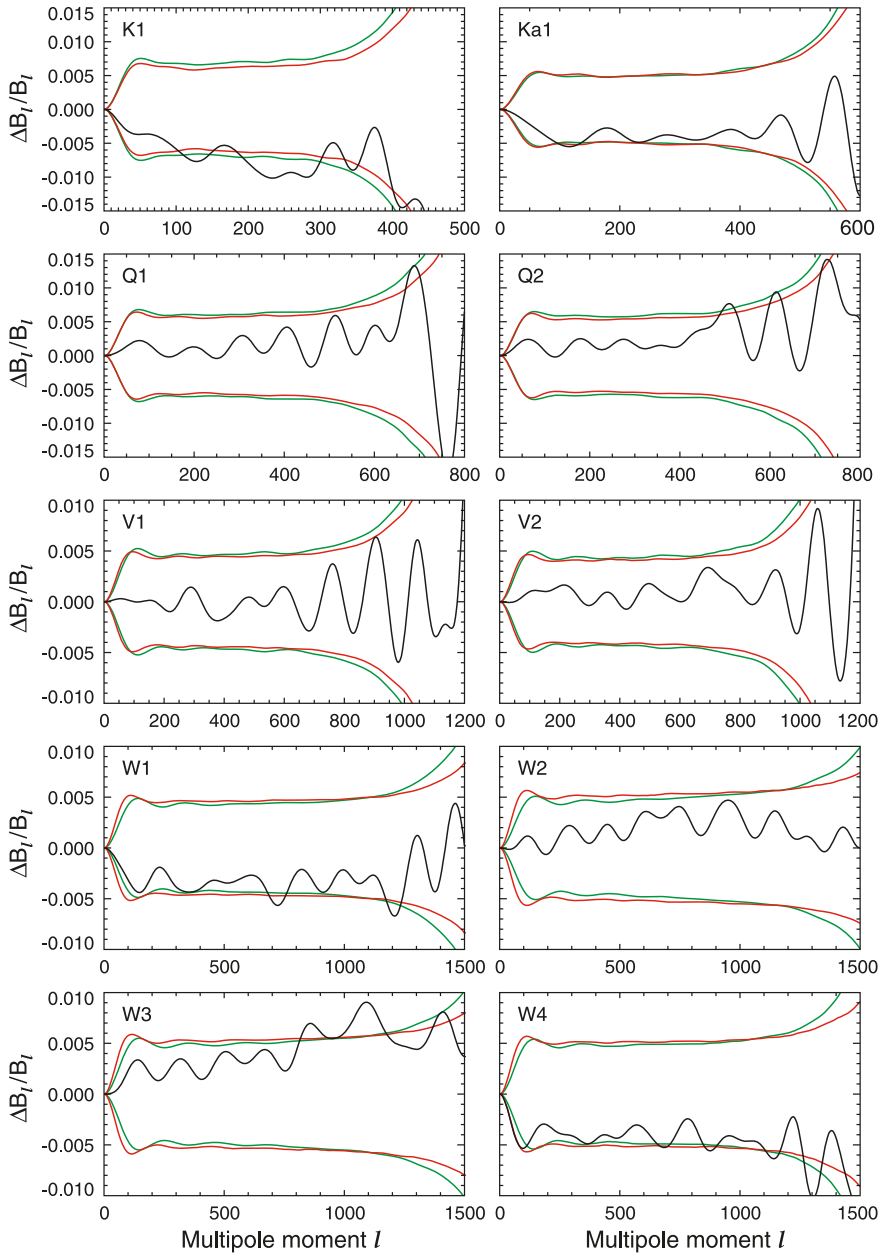

Fig. 4.— Comparison of beam transfer functions and uncertainties between five-year and seven-year analyses. *Black*: Relative change in beam transfer functions from five to seven years in the sense (7 yr − 5 yr)/(5 yr). *Green*: five-year 1σ error envelope. *Red*: seven-year 1σ error envelope. The seven-year b_ℓ are largely within 1σ of the five-year b_ℓ, while the change in the error envelope itself is small. In W band, modeling differences between the A and B sides introduce an increase in the uncertainty plateau for multipoles $\ell \lesssim 1000$, whereas the small angle (high ℓ) uncertainty is decreased for all bands.

The effective solid angle is calculated as

$$\Omega_{eff} = \Omega(Jupiter)\Omega_{GEMAC}(\beta)/\Omega_{GEMAC}(Jupiter) \tag{23}$$

where $\Omega(Jupiter)$ is the pass 4 beam solid angle determined from Jupiter observations and $\Omega(GEMAC)$ is the beam solid angle calculated for a given source spectrum using the scattering-corrected GEMAC measurements. From eq (25) of Page et al. (2003b),

$$\Omega(GEMAC) = 4\pi \int f(\nu)\nu^{\beta} d\nu / \int f(\nu) G_m(\nu)\nu^{\beta} d\nu \tag{24}$$

Values of ν_{eff}, Ω_{eff}, and Γ for a point source with $\beta = -2.1$, typical for the sources in the WMAP point source catalog, are given in Table 2.

4. Sky Map Data and Analysis

The seven-year sky maps are consistent with the 5 year maps apart from small effects related to the new processing methods. Figure 5 displays the seven-year band average Stokes I maps and the differences between these maps and the published five-year maps. The difference maps have been adjusted to compensate for the slightly different gain calibrations and dipole signals used in the different analysis. The small Galactic plane features in the K, Ka and Q band difference maps arise from the slightly different calibrations and small changes in the effective beam shapes. Pixels in the Galactic plane region are observed over a slightly smaller range of azimuthal beam orientation in the current data processing relative to previous analyses, resulting in slightly less azimuthal averaging and hence a slightly altered effective beam shape. The calibration gain changes relative to the five-year data release are small, all below 0.15% as indicated in Table 1.

4.1. The Temperature and Polarization Power Spectra

4.1.1. The Temperature Dipole and Quadrupole

The five-year CMB dipole value was obtained using a Gibbs sampling method (Hinshaw et al. 2009) to estimate the dipole signal in both the five-year Internal Linear Combination map (ILC) and foreground reduced maps. The uncertainties on the measured parameters were set to encompass both results as an estimate of the effect of residual foreground signals. The dipole measured from the seven-year data shows no significant changes from that obtained

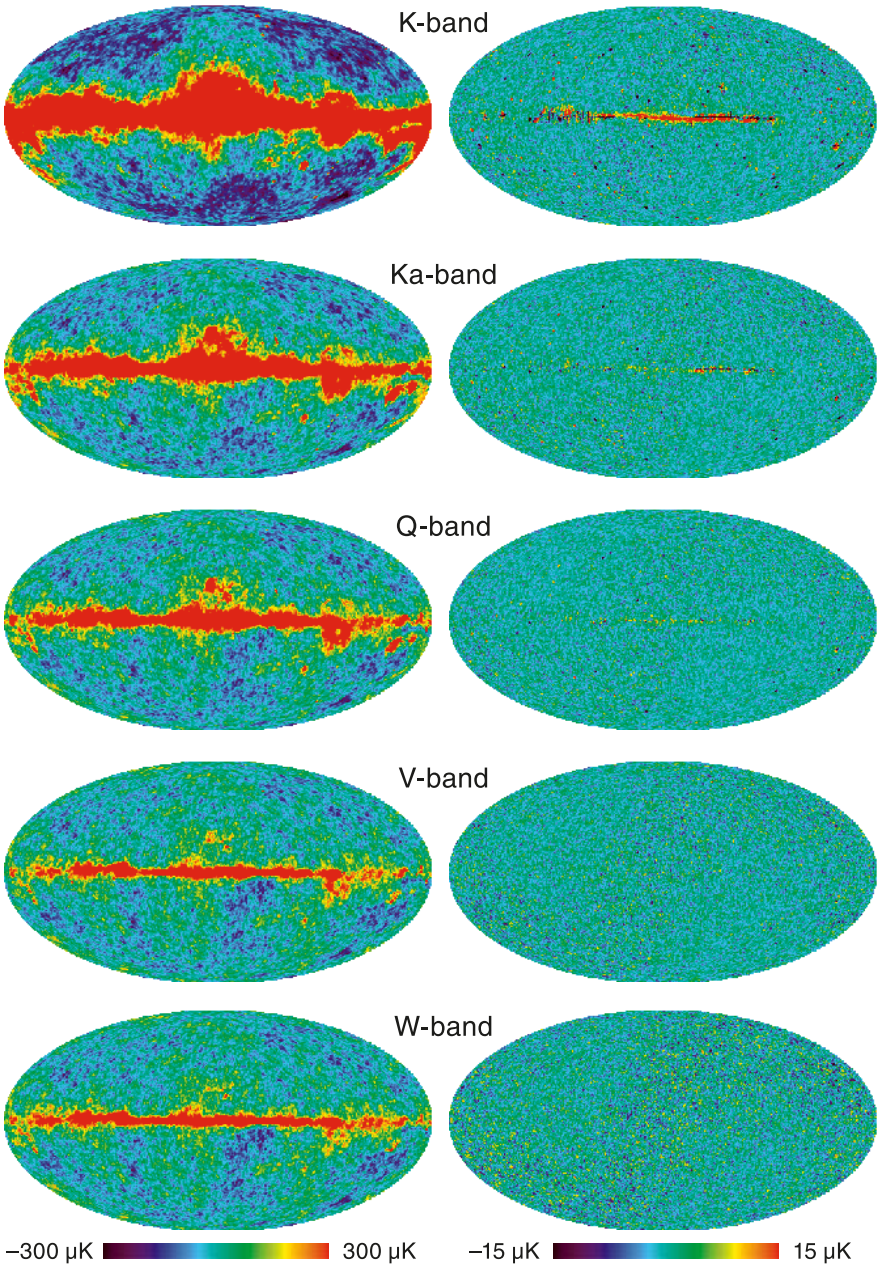

Fig. 5.— Plots of the Stokes I maps in Galactic coordinates. The left column displays the seven-year average maps, all of which have a common dipole signal removed. The right column displays the difference between the seven-year average maps and the previously published five-year average maps, adjusted to take into account the slightly different dipoles subtracted in the seven-year and five-year analyses and the slightly differing calibrations. All maps have been smoothed with a 1° FWHM Gaussian kernel. The small Galactic plane signal in the difference maps arises from the difference in calibration (0.1%) and beam symmetrization between the five-year and seven-year processing. Note that the temperature scale has been expanded by a factor of 20 for the difference maps.

from the five-year data, so the best fit dipole parameters remain unchanged from the five-year values, and are presented in Table 6.

The maximum likelihood value of magnitude of the CMB quadrupole is $l(l+1)C_l/2\pi = 197^{+2972}_{-155}\mu\mathrm{K}^2$ (95% CL) (Larson et al. 2010) based on analysis of the ILC map using the *KQ85* mask. This value is essentially unchanged from the five-year results and lies below the most likely value predicted by the best fit ΛCDM model. This value, however, is not particularly unlikely given the distribution of values predicted by the model, as described in Bennett et al. (2010).

Figure 6 displays the seven-year band average maps for Stokes Q and U components for all 5 *WMAP* frequency bands. Polarized Galactic emission is evident in all frequency bands. The smooth large angular scale features visible in the W-band maps, and to a lesser degree in the V-band maps, are the result of a pair of modes that are poorly constrained by the map-making procedure. While these dominate the appearance of the map, they are properly de-weighted when these maps are analyzed using their corresponding $\mathbf{\Sigma^{-1}}$ matrices, so useful polarization power spectra may be obtained from these maps. The relatively large amplitudes of these modes limits the utility of using difference plots between the five-year and seven-year map sets to test for consistency.

4.1.2. Low-ℓ W-band Polarization Spectra

Previous analyses (Hinshaw et al. 2009; Page et al. 2007) exhibited unexplained artifacts in the low-ℓ W-band polarization power spectra demonstrating an incomplete understanding of the signal and/or noise proprieties of these spectra. Specifically the value of C_ℓ^{EE} for $\ell = 7$ measured in W-band was found to be significantly higher than could be accommodated by the best fit power spectra, given the measurement uncertainty. This result, and several other anomalies, caused these data to be excluded from cosmological analyses. Significant effort has been expended trying to understand these spectra with the goal of eventually allowing their use in cosmological analyses.

A set of null spectra were formed based on the latest uncleaned W-band polarization sky maps to test for year-to-year and DA-to-DA consistency. Polarization cross power spectra were calculated for pairs of maps using the Master algorithm (Hivon et al. 2002) utilizing the full $\mathbf{\Sigma^{-1}}$ covariance matrix to weight the input maps. The polarization analysis mask was applied by marginalizing the $\mathbf{\Sigma^{-1}}$ over pixels excluded by the mask to minimize foreground contamination. Appropriately weighted null signal combinations of these spectra were formed to determine if any individual years or DAs possessed peculiar characteristics.

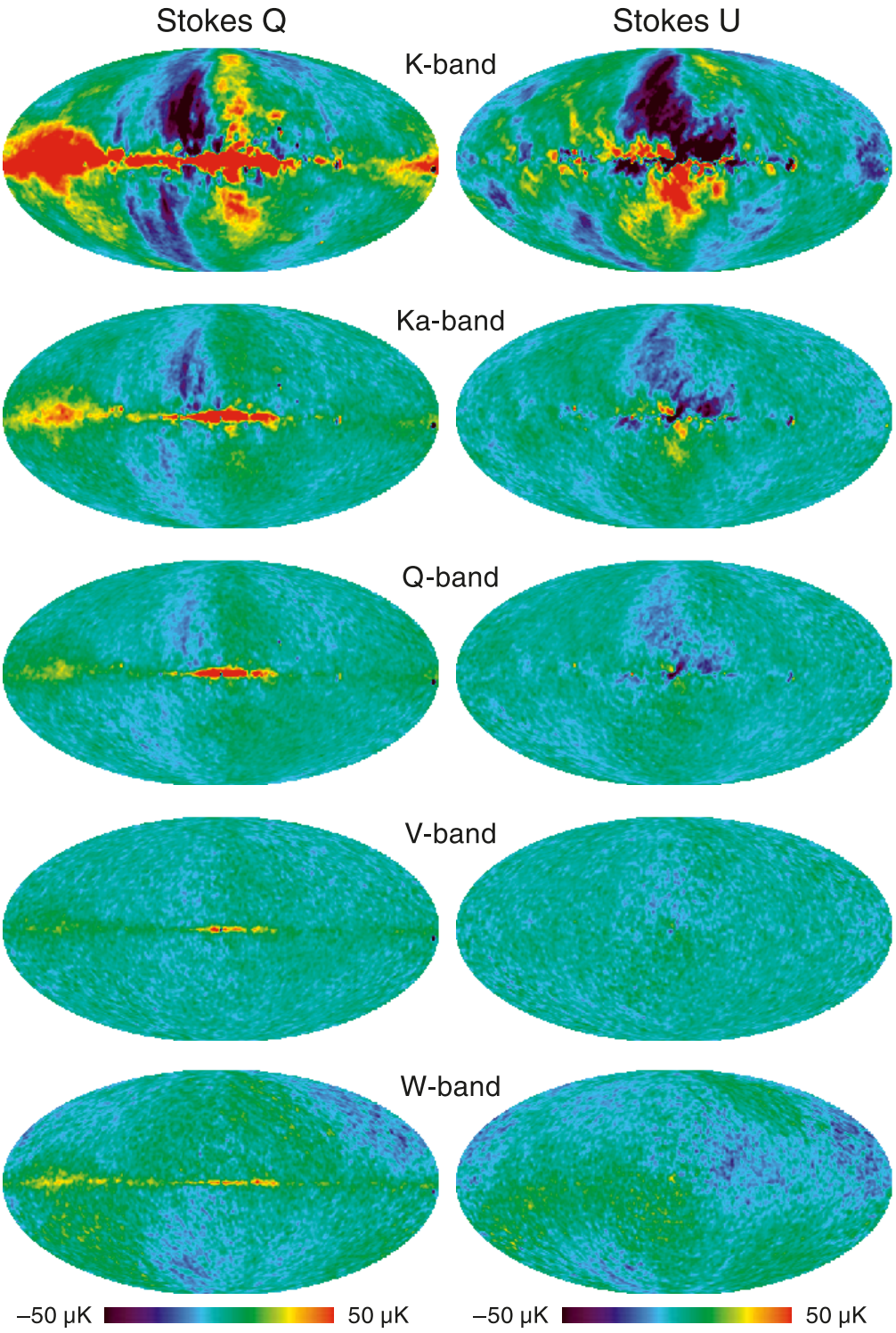

Fig. 6.— Plots of the Seven-year average Stokes Q and U maps in Galactic coordinates. All maps have been smoothed with a 2° FWHM Gaussian kernel.

The uncertainties on the power spectra were evaluated using the Fisher matrix technique (Page et al. 2007) and measured map noise levels. Since the input sky maps contain both signal (mostly of Galactic origin) and noise, an additional term was added to the Fisher matrix noise estimate to account for the signal $\times$ noise cross term. The signal component of this term was estimated using the seven-year average power spectra values for the combined W1, W2, and W3 DAs. This term was only added for multipole/polarization combinations (EE or BB) for which the estimated signal was greater than 0.

Table 7 shows the result of this analysis. The reduced χ^2 combinations in the top panel are evaluated for data combinations of all 4 W-band DAs that compare individual years to the average of the remaining years. Polarization combinations EE and BB were evaluated for multipoles ranging from 2-32. Additional combinations were formed to compare the first three years of data to the latter four, and to compare data taken in odd and even numbered years. All combinations resulted in reasonable χ^2 and probability to exceed values.

The lower half of the table contains the results of a similar analysis, but in this case combinations were formed to isolate individual DAs. The W4 is singled out with a reduced χ^2 value of 1.163 which has only a probability to exceed of only 0.05%. This DA has an unusually large 1/f knee frequency, which makes it particularly susceptible to systematic artifacts. For this reason it is excluded from the analysis below, but continues to be studied in case it might contain clues as to the nature of the low-ℓ polarization anomalies seen in the other W-band DAs.

Figure 7 displays polarization power spectra for the EE, BB and EB modes for the first three, five, and seven years of template cleaned individual year maps from the W1, W2 and W3 DAs. These spectra were also obtained using the Master algorithm utilizing the mask-marginalized $\mathbf{\Sigma^{-1}}$ covariance matrix sky map weighting. Only cross power spectra are included, so the measurement noise does not bias the measured values. The uncertainties are based on the Fisher matrix technique, and have not had the signal $\times$ noise term added, since any signal remaining in the cleaned maps is expected to be small. (Master algorithm based low-ℓ power spectra are not used in any cosmological analyses.)

There is generally good agreement between the values for the three different time ranges. Note that the high value seen in the three and five-year analysis for $C_7^{\rm EE}$ has fallen significantly with the additional two years of data. In fact, had the data been take in reverse order (starting with year seven) the $C_7^{\rm EE}$ value would not have been identified as particularly anomalous. However, the $C_{12}^{\rm EE}$ value has risen in the seven-year combination. To see if these signals might be artifacts of the foreground cleaning, a similar analysis was performed on the uncleaned sky maps and is displayed in Figure 8. By comparing the two figures it can be seen that the foreground cleaning mainly affects the multipoles $\ell \leq 5$ leaving the $\ell = 7, 12$

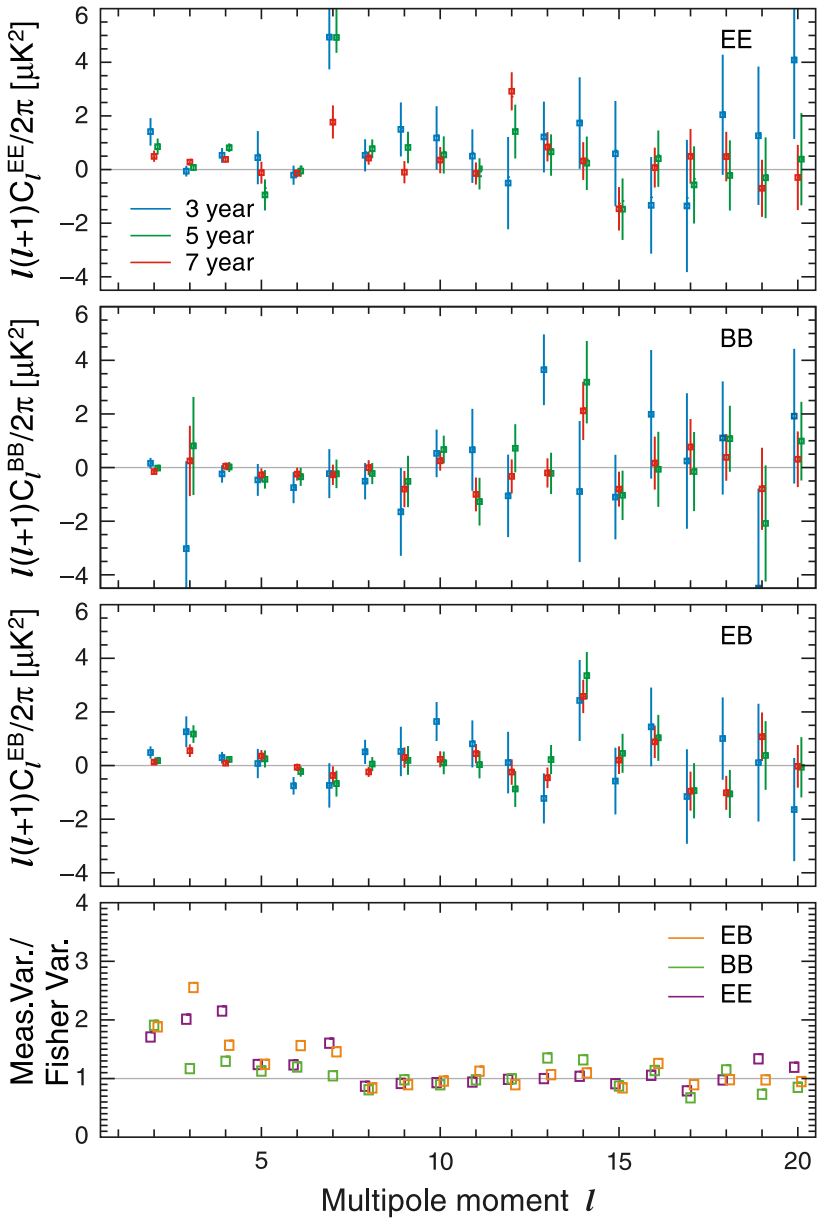

Fig. 7.— Low ℓ Master polarization cross power spectra from the first three, five, and seven years of data from the W1, W2 and W3 foregrounds reduced polarization sky maps (Gold et al. 2010) for the first three, five and seven years of observations. These three time ranges contain 36, 105 and 210 individual cross spectra respectively. The ℓ values for the different time ranges have been offset for clarity. The top three panels contain the Master power spectra and error bars based on a Fisher matrix analysis. The bottom panel is the ratio of the measured variance between the individual power spectra estimates (DA year $\times$ DA year) and the variance predicted by the Fisher matrix calculation using the full Σ^{-1} inverse noise covariance matrix. Note the good agreement for $\ell \geq 8$.

multipoles relatively unchanged.

The bottom panel of these figures plot the ratio between the variance measured among the individual cross spectra for each multipole/polarization combination, to that predicted by the Fisher matrix technique. For $\ell \geq 8$ there is good agreement between the measured variance and analytical estimate, but the measured variance slowly grows larger with decreasing ℓ for $\ell \leq 7$ for both the cleaned and uncleaned sky maps. The Fisher matrix noise estimate utilizes the $\mathbf{\Sigma^{-1}}$ matrix that describes the noise correlation between the pixels of the Stokes Q and U maps. This matrix incorporates information regarding the sky scanning pattern, through the mapping matrices $\mathbf{M}$ and $\mathbf{M}_{\rm am}$, and correlations in the radiometer noise, through the use of inverse radiometer noise covariance matrix $\mathbf{N^{-1}}$. This method does not, however, include the effect of any noise correlations that might be introduced through the baseline fitting and calibration procedure. A program was undertaken to determine if the baseline fitting and calibration procedure could be affecting the low-ℓ polarization results and is described in the following section.

4.1.3. Calibration Induced Spectral Uncertainties

Uncertainties in the polarization power spectra arising from calibration of the TOD were evaluated using the Fisher information matrix method . New sets of noise matrices were calculated including degrees of freedom associated with the gain and baseline parameters used in the calibration procedure. The values of these two parameters were approximated as piecewise functions, each assumed constant over one hour intervals. The calibration procedure was modeled as a χ^2 minimization of the residuals between the TOD and a predicted TOD calculated by applying the gain and baseline values for each time interval to a model signal consisting of CMB anisotropy and a time dependent dipole due to *WMAP* 's motion about the solar system barycenter. Fisher information matrices were calculated for this model and inverted to form noise matrices. Uncertainties in the recovered low-ℓ power spectra were calculated using this method by marginalizing over the values of the gain and baseline parameters. A similar calculation was performed with the gain and baseline terms omitted. The effects of the calibration on the uncertainties in the recovered power spectra were measured by comparing the results of these two calculations.

As expected, the difference in the predicted uncertainties was small for all but the very lowest multipoles. This occurs because the signal from the low-ℓ multipoles enters the TOD on the longest time scales, and therefore is most affected by a the calibration procedure which fits the low frequency dipole signal used for calibration. For E-mode polarization the maximum increase in uncertainty in a_{lm} is about 3.5% occurring for $\ell = 3$ and is less than

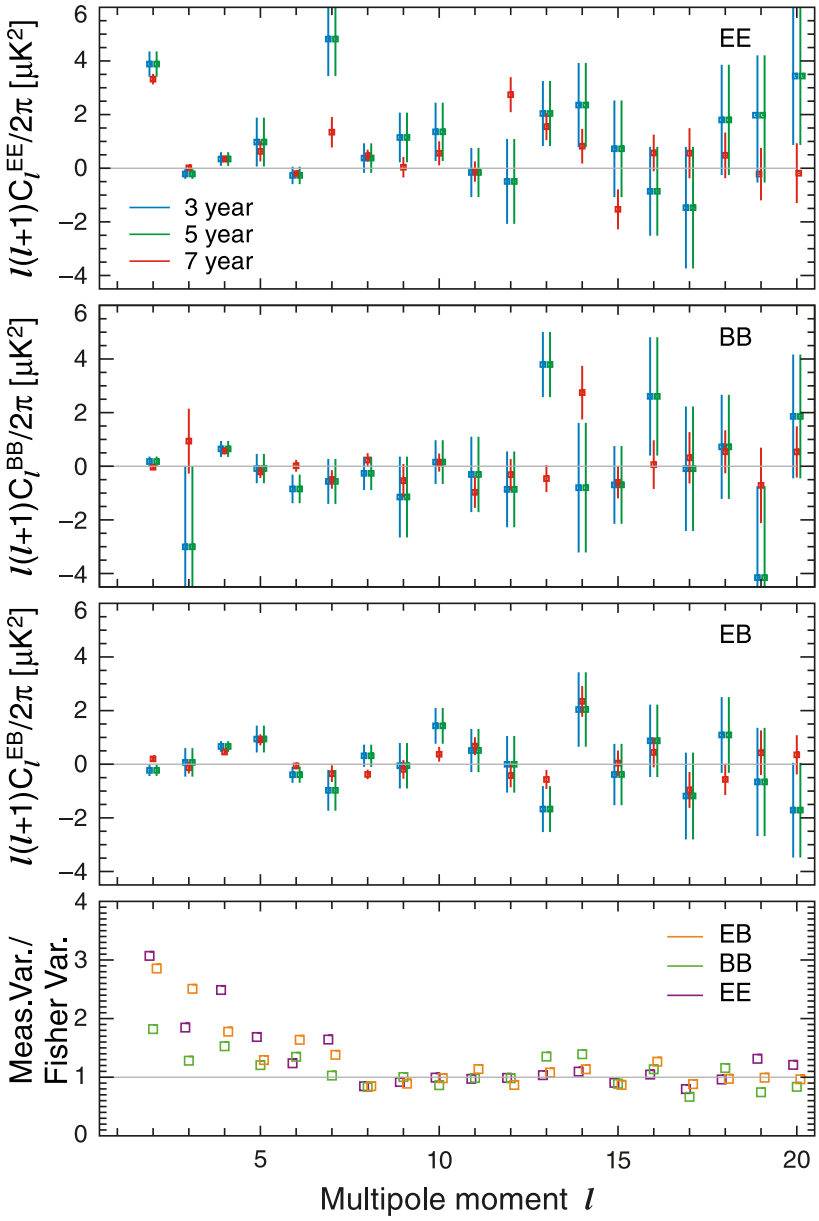

Fig. 8.— Low ℓ Master polarization cross power spectra from the first three, five, and seven years of data from the W1, W2 and W3 uncleaned sky maps. The ℓ values have been offset slightly for the different time ranges for clarity. The bottom panel is the ratio of the measured variance between the individual power spectra estimates (DA year $\times$ DA year) and the variance predicted from a Fisher matrix calculation using the full Σ^{-1} inverse noise covariance matrix. Note the good agreement for $\ell \geq 8$.

1% for other multipoles. For the B-mode a_{lm} uncertainties for $\ell = 2, 3$ increase by 40% and 90% respectively, while the effect on other multipoles is less that 1%. The $\ell = 3$ B-mode polarization was already known to be very poorly measured by *WMAP* , since its symmetry, combined with *WMAP* 's geometry and scan pattern, generate extremely long period signals (periods exceeding 10 minutes) in the TOD. The fact that the calculation described above correctly identified this mode supports the validity of the methodology used, but the overall results do no fully explain the excess variance observed in all the W-band $\ell \leq 7$ polarization multipoles. The low-ℓ W-band polarization data therefore continue to be excluded from cosmological analysis. However, there is no evidence suggesting any compromise of the high-ℓ W-band polarization data, so it it now included in evaluation of the high-ℓ TE power spectrum.

4.2. Science Highlights

The *WMAP* data remains one of the cornerstone data sets used for testing the cosmological models and the precision measurement of their parameters. Figure 9 displays the binned TT and TE angular power spectra measured from the seven-year *WMAP* data (Larson et al. 2010), along with the predicted spectrum for the best fit minimal six-parameter flat ΛCDM model. The overall agreement is excellent, supporting the validity of this model. Table 8 tabulates the parameter values for this model using *WMAP* data alone, and in combination with other data sets. Details of the methodology used to determine these values are described in Larson et al. (2010) and Komatsu et al. (2010).

The seven-year *WMAP* results significantly reduce the uncertainties for numerous cosmological parameters relative to the five-year results. The uncertainties in the densities of baryonic and dark matter are reduced by 10% and 13% respectively. When tensor modes are included, the upper bound to their amplitude, determined using *WMAP* data alone, is nearly 20% lower. By combining *WMAP* data with the latest distance measurements from Baryon Acoustic Oscillations (BAO) in the distribution of galaxies (Percival et al. 2009) and Hubble constant measurements (Riess et al. 2009), the spectral index of the power spectrum of primordial curvature perturbations is $n_s = 0.963 \pm 0.012$, excluding the Harrison-Zel'dovich-Peebles spectrum by more than 3σ.

The reduced noise obtained by using the seven-year data set yields a better measurement of the third acoustic peak in the temperature power spectrum. This measurement, when combined with external data sets, leads to better determinations of the total mass of neutrinos, $\sum m_\nu$, and the effective number of neutrino species, $N_{\rm eff}$, as presented in Table 8. Additionally, when augmented by the small scale CMB anisotropy measurements by ACBAR

(Reichardt et al. 2009) and QUaD (Brown et al. 2009), this result yields a greater that 3σ detection of the primordial Helium abundance, $Y_{\rm He} = 0.326 \pm 0.075$, using CMB data alone. Komatsu et al. (2010) also demonstrate that, with the larger data set, the expected radial and azimuthal polarization patterns around hot and cold peaks in the CMB can now be observed directly in pixel-space by stacking sky map data. In addition, they now detect the Sunyaev-Zel'dovich effect at $\approx 8\sigma$ at the location of known galaxy clusters, as determined by ROSAT.

Finally, Weiland et al. (2010) have measured the brightness temperature of Jupiter, Saturn, Mars, Uranus and Neptune, and five fixed calibrations objects, in all five frequency bands, allowing their use as mm-wave celestial calibration sources traceable to *WMAP* 's precise calibration.

5. Summary

The *WMAP* observatory has successfully completed seven years of observations with no significant performance degradation. A full set of sky maps for the seven year data span has been generated and are available for analyses by the astrophysical community. These maps were generated with an updated masking procedure that simplifies the map-making procedure and allows creation of a single full-sky noise correlation matrix describing the noise correlation over the entire sky for the reduced resolution sky maps. The understanding of the beam profiles and resulting window functions has been improved with the additional bean profile information obtained by more observations of Jupiter. The planetary observations, combined with the precise absolute calibration of *WMAP* , were used to measure the brightness temperature of Mars, Jupiter, Saturn, Uranus and Neptune for use as calibration sources.

Finally, the additional data and a better understanding of the instrument's characteristics has resulted in tighter constraints on the value of parameters of cosmological models.

WMAP is funded by the Science Mission Directorate Office at NASA Headquarters. We acknowledge use of the HEALPix (Gorski et al. 2005) software package. The numerous data products described in this document are available from the Legacy Archive for Microwave Background Data Analysis (LAMBDA) `http://lambda.gsfc.nasa.gov`.

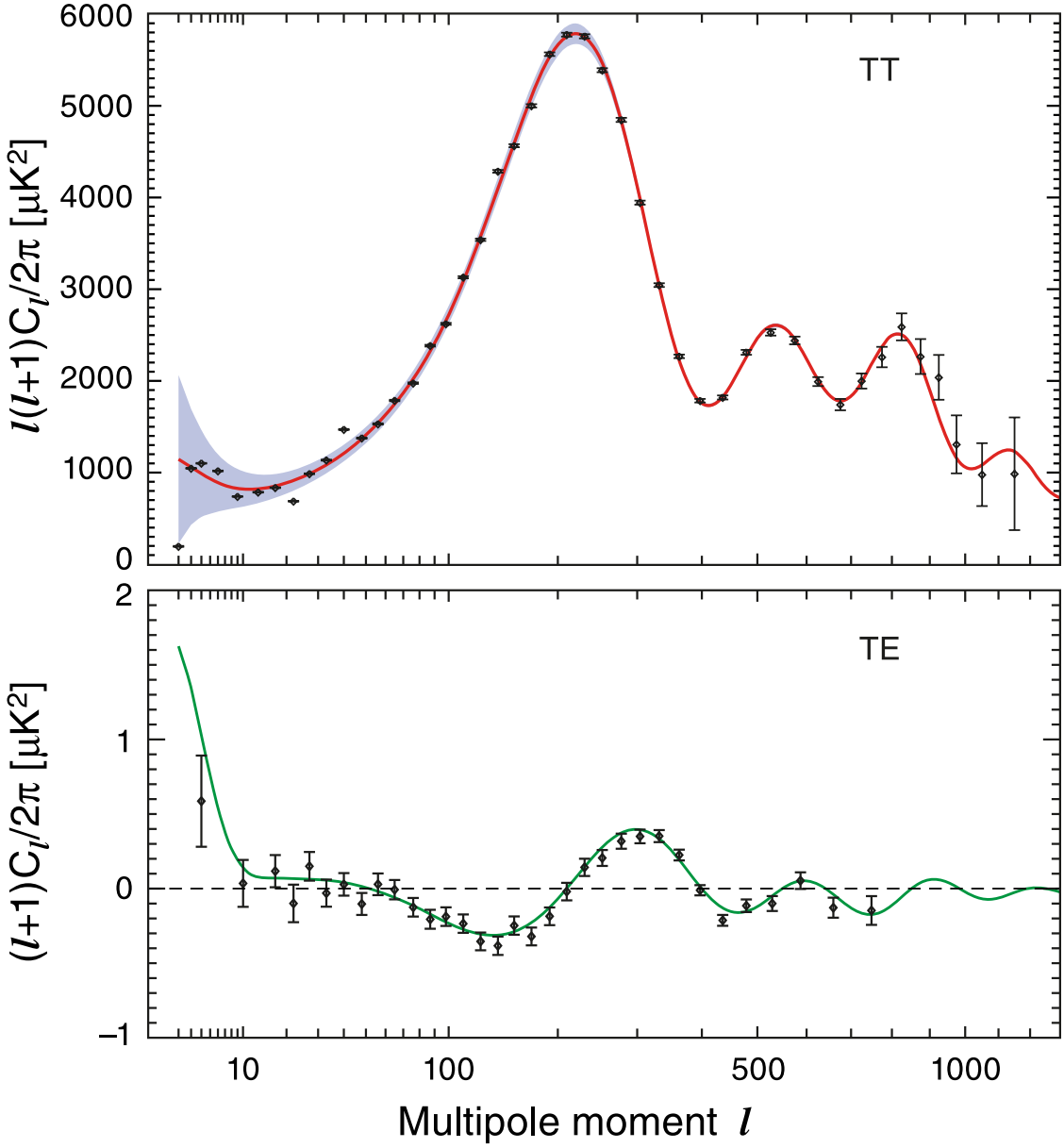

Fig. 9.— The temperature (TT) and temperature-polarization(TE) power spectra for the seven-year *WMAP* data set. The solid lines show the predicted spectrum for the best-fit flat ΛCDM model. The error bars on the data points represent measurement errors while the shaded region indicates the uncertainty in the model spectrum arising from cosmic variance. The model parameters are: $\Omega_b h^2 = 0.02260 \pm 0.00053$, $\Omega_c h^2 = 0.1123 \pm 0.0035$, $\Omega_\Lambda = 0.728^{+0.015}_{-0.016}$, $n_s = 0.963 \pm 0.012$, $\tau = 0.087 \pm 0.014$ and $\sigma_8 = 0.809 \pm 0.024$.

Table 3. Seven-year Transmission Imbalance Coefficients

Radiometer	$x_{\rm im}$	Uncertainty	Radiometer	$x_{\rm im}$	Uncertainty
K11	-0.00063	0.00022	K12	0.00539	0.00010
Ka11	0.00344	0.00017	Ka12	0.00153	0.00011
Q11	0.00009	0.00051	Q12	0.00393	0.00025
Q21	0.00731	0.00058	Q22	0.01090	0.00116
V11	0.00060	0.00025	V12	0.00253	0.00068
V21	0.00378	0.00033	V22	0.00331	0.00106
W11	0.00924	0.00207	W12	0.00145	0.00046
W21	0.00857	0.00227	W22	0.01167	0.00154
W31	-0.00073	0.00062	W32	0.00465	0.00054
W41	0.02314	0.00461	W42	0.02026	0.00246

Note. — Transmission imbalance coefficients, $x_{\rm im}$, and their uncertainties determined from the seven-year observational data.

Table 4. *WMAP* Seven-year Main Beam Parameters

DA	$\Omega^S_{7\rm yr}$ [a] (sr)	$\Delta(\Omega^S_{7\rm yr})/\Omega^S$ [b] (%)	$\frac{\Omega^S_{7\rm yr}}{\Omega^S_{5\rm yr}} - 1$ [c] (%)	G_m [d] (dBi)	$\nu^{\rm ff}_{\rm eff}$ (GHz)	$\Omega^{\rm ff}_{\rm eff}$ (sr)	$\Gamma_{\rm ff}$ [e] (μK Jy^{-1})
		For 10 Maps					
K1	2.466×10^{-4}	0.6	0.8	47.07	22.72	2.519×10^{-4}	250.3
Ka1	1.442×10^{-4}	0.5	0.4	49.40	32.98	1.464×10^{-4}	204.5
Q1	8.832×10^{-5}	0.6	-0.1	51.53	40.77	8.952×10^{-5}	218.8
Q2	9.123×10^{-5}	0.5	-0.2	51.39	40.56	9.244×10^{-5}	214.1
V1	4.170×10^{-5}	0.4	0.0	54.79	60.12	4.232×10^{-5}	212.8
V2	4.234×10^{-5}	0.4	-0.1	54.72	61.00	4.281×10^{-5}	204.4
W1	2.042×10^{-5}	0.4	0.2	57.89	92.87	2.044×10^{-5}	184.6
W2	2.200×10^{-5}	0.5	-0.3	57.57	93.43	2.200×10^{-5}	169.5
W3	2.139×10^{-5}	0.5	-0.5	57.69	92.44	2.139×10^{-5}	179.0
W4	2.007×10^{-5}	0.5	0.5	57.97	93.22	2.010×10^{-5}	186.4
		For 5 Maps					
K	2.466×10^{-4}	0.6	0.8	47.07	22.72	2.519×10^{-4}	250.3
Ka	1.442×10^{-4}	0.5	0.4	49.40	32.98	1.464×10^{-4}	204.5
Q	8.978×10^{-5}	0.6	-0.2	51.46	40.66	9.098×10^{-5}	216.4
V	4.202×10^{-5}	0.4	-0.1	54.76	60.56	4.256×10^{-5}	208.6
W	2.097×10^{-5}	0.5	0.0	57.78	92.99	2.098×10^{-5}	179.3

[a]Solid angle in azimuthally symmetrized beam.

[b]Relative error in Ω^S.

[c]Relative change in Ω^S between five-year and seven-year analyses.

[d]Forward gain = maximum of gain relative to isotropic, defined as $4\pi/\Omega^S$. Values of G_m in Table 2 of Hill et al. (2009) were taken from the physical optics model, rather than computed from the solid angle, and therefore do not obey this relation.

[e]Conversion factor to obtain flux density from the peak *WMAP* antenna temperature, for a free-free spectrum with $\beta = -2.1$. Uncertainies in these factors are estimated as 0.6, 0.5, 0.6, 0.5 and 0.7% for K, Ka, Q, V and W band DAs respectively.

Table 5. Changes in χ^2 from five-year to seven-year beam fits

DA	χ^2_ν (5 year)	χ^2_ν (7 year)	$\Delta\chi^2_\nu$
	Side A		
all	1.060	1.049	-0.011
K1	1.009	1.006	-0.004
Ka1	1.012	1.016	0.004
Q1	1.078	1.074	-0.003
Q2	1.094	1.102	0.008
V1	1.144	1.155	0.011
V2	1.162	1.171	0.008
W1	1.225	1.171	-0.053
W2	1.239	1.151	-0.088
W3	1.244	1.181	-0.063
W4	1.208	1.156	-0.052
	Side B		
all	1.065	1.047	-0.018
K1	1.022	1.017	-0.005
Ka1	1.010	1.009	-0.000
Q1	1.093	1.046	-0.046
Q2	1.045	1.052	0.007
V1	1.288	1.171	-0.117
V2	1.178	1.159	-0.019
W1	1.226	1.197	-0.029
W2	1.169	1.155	-0.013
W3	1.223	1.203	-0.021
W4	1.226	1.165	-0.061

Table 6. *WMAP* Seven-Year CMB Dipole Parameters

d_x[a] (mK)	d_y (mK)	d_z (mK)	d[b] (mK)	l (°)	b (°)
-0.233 ± 0.005	-2.222 ± 0.004	2.504 ± 0.003	3.355 ± 0.008	263.99 ± 0.14	48.26 ± 0.03

Note. — The measured values of the CMB dipole signal. These values are unchanged from the five-year values and are reproduced here for completeness.

[a]Cartesian components are give in Galactic coordinates. The listed uncertainties include the effects of noise, masking and residual foreground contamination. The 0.2% absolute calibration uncertainty should be added to these values in quadrature.

[b]The spherical components of the CMB dipole are given in Galactic coordinates and already include all uncertainty estimates, including the 0.2% absolute calibration uncertainty.

Table 7. Seven-year Spectrum χ^2 W-band Null Tests

Data Combinations	$\chi^2_{\rm EE}$	$PTE_{\rm EE}$	$\chi^2_{\rm BB}$	$PTE_{\rm BB}$
For DAs W1, W2, W3 and W4				
{yr1} - {y2, y3, y4, y5, y6, y7}	0.944	0.56	0.976	0.50
{yr2} - {y1, y3, y4, y5, y6, y7}	0.800	0.78	0.956	0.54
{yr3} - {y1, y2, y4, y5, y6, y7}	0.934	0.57	1.166	0.24
{yr4} - {y1, y2, y3, y5, y6, y7}	0.850	0.70	0.920	0.59
{yr5} - {y1, y2, y3, y4, y6, y7}	0.737	0.85	1.286	0.13
{yr6} - {y1, y2, y3, y4, y5, y7}	0.769	0.82	1.101	0.32
{yr7} - {y1, y2, y3, y4, y5, y6}	1.108	0.31	0.831	0.73
{yr1, yr2, y3} - {y4, y5, y6, y7}	0.608	0.96	0.98	0.49
{yr1, yr3, y5, y7} - {y2, y4, y6}	0.860	0.69	1.06	0.38
For 7 years of data				
{W1} - {W2, W3, W4}	1.195	0.21	0.982	0.49
{W2} - {W1, W3, W4}	0.802	0.77	0.926	0.58
{W3} - {W1, W2, W4}	0.890	0.64	0.897	0.63
{W4} - {W1, W2, W3}	1.163	0.24	2.061	0.0005
{W1, W2} - {W3, W4}	0.867	0.68	1.361	0.09
{W1, W3} - {W2, W4}	0.866	0.68	1.219	0.19

Note. — χ^2 tests for various null combinations of low-ℓ Master polarization power spectra obtained from uncleaned W-band sky maps. Reduced χ^2 values are presented along with the probability to exceed (PTE) values based on 31 degrees of freedom, corresponding to $2 \leq \ell \leq 32$. Polarization cross power spectra were obtained for each DA year $\times$ DA year combination, then appropriately weighted combinations generated to null any sky signal. Predicted uncertainties were obtained using the standard Fisher matrix formalism incorporating the inverse noise covariance matrices and the measured sky map noise levels. Since individual power spectra estimates do include signals (mostly foreground), the uncertainties include a contribution for the signal $\times$ noise cross term as explained in the text. The only anomalous point occurs when the seven-year W4 data is compared to the seven-year data from the remaining W-band DAs.

Table 8. *WMAP* Seven-year Cosmological Parameter Summary

Description	Symbol	*WMAP* -only	*WMAP* +BAO+H_0
Parameters for Standard ΛCDM Model [a]			
Age of universe	t_0	13.75 ± 0.13 Gyr	13.75 ± 0.11 Gyr
Hubble constant	H_0	71.0 ± 2.5 km/s/Mpc	$70.4^{+1.3}_{-1.4}$ km/s/Mpc
Baryon density	Ω_b	0.0449 ± 0.0028	0.0456 ± 0.0016
Physical baryon density	$\Omega_b h^2$	$0.02258^{+0.00057}_{-0.00056}$	0.02260 ± 0.00053
Dark matter density	Ω_c	0.222 ± 0.026	0.227 ± 0.014
Physical dark matter density	$\Omega_c h^2$	0.1109 ± 0.0056	0.1123 ± 0.0035
Dark energy density	Ω_Λ	0.734 ± 0.029	$0.728^{+0.015}_{-0.016}$
Curvature fluctuation amplitude, $k_0 = 0.002$ Mpc^{-1} [b]	$\Delta^2_{\mathcal{R}}$	$(2.43 \pm 0.11) \times 10^{-9}$	$(2.441^{+0.088}_{-0.092}) \times 10^{-9}$
Fluctuation amplitude at $8h^{-1}$ Mpc	σ_8	0.801 ± 0.030	0.809 ± 0.024
Scalar spectral index	n_s	0.963 ± 0.014	0.963 ± 0.012
Redshift of matter-radiation equality	$z_{\rm eq}$	3196^{+134}_{-133}	3232 ± 87
Angular diameter distance to matter-radiation eq.[c]	$d_A(z_{\rm eq})$	14281^{+158}_{-161} Mpc	14238^{+128}_{-129} Mpc
Redshift of decoupling	z_*	$1090.79^{+0.94}_{-0.92}$	$1090.89^{+0.68}_{-0.69}$
Age at decoupling	t_*	379164^{+5187}_{-5243} yr	377730^{+3205}_{-3200} yr
Angular diameter distance to decoupling [c,d]	$d_A(z_*)$	14116^{+160}_{-163} Mpc	14073^{+129}_{-130} Mpc
Sound horizon at decoupling [d]	$r_s(z_*)$	$146.6^{+1.5}_{-1.6}$ Mpc	146.2 ± 1.1 Mpc
Acoustic scale at decoupling [d]	$l_A(z_*)$	302.44 ± 0.80	302.40 ± 0.73
Reionization optical depth	τ	0.088 ± 0.015	0.087 ± 0.014
Redshift of reionization	$z_{\rm reion}$	10.5 ± 1.2	10.4 ± 1.2
Parameters for Extended Models [e]			
Total density [f]	$\Omega_{\rm tot}$	$1.080^{+0.093}_{-0.071}$	$1.0023^{+0.0056}_{-0.0054}$
Equation of state [g]	w	$-1.12^{+0.42}_{-0.43}$	-0.980 ± 0.053
Tensor to scalar ratio, $k_0 = 0.002$ Mpc^{-1} [b,h]	r	< 0.36 (95% CL)	< 0.24 (95% CL)
Running of spectral index, $k_0 = 0.002$ Mpc^{-1} [b,i]	$dn_s/d\ln k$	-0.034 ± 0.026	-0.022 ± 0.020
Neutrino density [j]	$\Omega_\nu h^2$	< 0.014 (95% CL)	< 0.0062 (95% CL)
Neutrino mass [j]	$\sum m_\nu$	< 1.3 eV (95% CL)	< 0.58 eV (95% CL)
Number of light neutrino families [k]	$N_{\rm eff}$	> 2.7 (95% CL)	$4.34^{+0.86}_{-0.88}$

[a]The parameters reported in the first section assume the 6 parameter flat ΛCDM model, first using *WMAP* data only (Larson et al. 2010), then using *WMAP* +BAO+H_0 data (Komatsu et al. 2010). The H_0 data consists of a Gaussian prior on the present-day value of the Hubble constant, $H_0 = 74.2 \pm 3.6$ km s^{-1} Mpc^{-1}(Riess et al. 2009), while the BAO priors on the distance ratio $r_s(z_d)/D_{\rm V}(z)$ at $z = 0.2,\ 0.3$ are obtained from the Sloan Digital Sky Survey Data Release 7 (Percival et al. 2009). Uncertainties are 68% CL unless otherwise noted.

[b]$k = 0.002$ Mpc^{-1} $\longleftrightarrow$ $l_{\rm eff} \approx 30$.

[c]Comoving angular diameter distance.

[d]$l_A(z_*) \equiv \pi\, d_A(z_*)\, r_s(z_*)^{-1}$.

[e]The parameters reported in the second section place limits on deviations from the ΛCDM model, first using *WMAP* data only (Larson et al. 2010), then using *WMAP* +BAO+H_0 data (Komatsu et al. 2010), except as noted otherwise. A complete listing of all parameter values and uncertainties for each of the extended models studied is available on LAMBDA.

[f]Allows non-zero curvature, $\Omega_k \neq 0$.

[g]Allows $w \neq -1$, but assumes w is constant and $\Omega_k = 0$. The value in the last column is obtained from a combination of *WMAP* +BAO data and luminosity distance information obtained from the "constitution" SNe data set (Hicken et al. 2009) using the methodology described in Komatsu et al. (2010)

[h]Allows tensors modes but no running in scalar spectral index.

[i]Allows running in scalar spectral index but no tensor modes.

[j]Allows a massive neutrino component, $\Omega_\nu \neq 0$.

[k]Allows $N_{\rm eff}$ number of relativistic species, with the prior $0 < N_{\rm eff} < 10$.

REFERENCES

Barrett, R., et al. 1994, Templates for the Solution of Linear Systems: Building Blocks for Iterative Methods, 2nd Edition (Philadelphia, PA: SIAM)

Bennett, C. L., et al. 2003a, ApJS, 148, 1

—. 2003b, ApJ, 583, 1

Bennett, C. L. et al. 2010, in preparation

Brown, M. L., et al. 2009, ApJ, 705, 978

Gold, B. et al. 2010, in preparation

Gorski, K. M., Hivon, E., Banday, A. J., Wandelt, B. D., Hansen, F. K., Reinecke, M., & Bartlemann, M. 2005, ApJ, 622, 759

Hicken, M., Wood-Vasey, W. M., Blondin, S., Challis, P., Jha, S., Kelly, P. L., Rest, A., & Kirshner, R. P. 2009, ApJ, 700, 1097

Hill, R. S., et al. 2009, ApJS, 180, 246

Hinshaw, G. et al. 2003, Astrophys. J. Suppl., 148, 63

Hinshaw, G., et al. 2009, ApJS, 180, 225

Hivon, E., Górski, K. M., Netterfield, C. B., Crill, B. P., Prunet, S., & Hansen, F. 2002, ApJ, 567, 2

Jarosik, N., et al. 2003, ApJS, 145, 413

—. 2007, ApJS, 170, 263

Komatsu, E. et al. 2010, in preparation

Larson, D. et al. 2010, in preparation

Limon, M., et al. 2010, Wilkinson Microwave Anisotropy Probe (*WMAP*): Seven Year Explanatory Supplement, `http://lambda.gsfc.nasa.gov/data/map/doc/MAP_supplement.pdf`

Mather, J. C., Fixsen, D. J., Shafer, R. A., Mosier, C., & Wilkinson, D. T. 1999, ApJ, 512, 511

Page, L., et al. 2003a, ApJS, 148, 39

—. 2003b, ApJ, 585, 566

—. 2007, ApJS, 170, 335

Percival, W. J., et al. 2009, MNRAS, 1741

Reichardt, C. L., et al. 2009, ApJ, 694, 1200

Riess, A. G., et al. 2009, ApJ, 699, 539

Weiland, J. L. et al. 2010, in preparation

This preprint was prepared with the AAS LaTeX macros v5.2.